Bulletin of the Seismological Society of America, Vol. 101, No. 1, pp. 79–92, February 2011, doi: 10.1785/0120100004

Estimating Earthquake-Rupture Rates on a Fault or Fault System

by Edward H. Field and Morgan T. Page

Abstract Previous approaches used to determine the rates of different earthquakes on a fault have made assumptions regarding segmentation, have been difficult to document and reproduce, and have lacked the ability to satisfy all available data constraints. We present a relatively objective and reproducible inverse methodology for determining the rate of different ruptures on a fault or fault system. The data used in the inversion include slip rate, event rate, and other constraints such as an optional *a priori* magnitude–frequency distribution. We demonstrate our methodology by solving for the long-term rate of ruptures on the southern San Andreas fault. Our results imply that a Gutenberg–Richter distribution is consistent with the data available for this fault; however, more work is needed to test the robustness of this assertion. More importantly, the methodology is extensible to an entire fault system (thereby including multifault ruptures) and can be used to quantify the relative benefits of collecting additional paleoseismic data at different sites.

Introduction

Probabilistic seismic hazard assessment requires the availability of models that give the long-term rate of different earthquake ruptures for each seismic source. Some of the most sophisticated models for fault-based sources have been developed by the recent Working Groups on California Earthquake Probabilities (WGCEP; 1988, 1990, 1995, 2003, and 2008). Although each of these studies represented state-of-the-art approaches, their fault-based models exhibit some shortcomings that may be important in terms of seismic-hazard implications. For example, the two most recent WGCEPs (2003 and 2008) both took the following general approach in developing models for the most well-characterized faults:

1. Assume segmentation—that is, divide the faults into a small number of large segments (e.g., four for the ~470 km northern San Andreas fault, based on previous earthquakes and fault complexity), and assume that earthquake ruptures involve all of one or more segments (never just part of any segment).
2. Convene an expert panel to examine paleoseismic and other data to come up with an estimate of the relative frequency (WGCEP, 2003) or absolute rate (WGCEP, 2008) of each single and multisegment rupture.
3. Adjust the models developed in step (2) by whatever minimal amount is necessary to make them moment balanced (consistent with fault slip-rate estimates).

The first problem with this approach is that segmentation may be incorrect (i.e., ruptures might actually begin and end at more than just a few locations along the fault), and, if so, this admittedly convenient approximation may be misleading in terms of the implied seismic hazard. The second problem is that deliberations by an expert panel are both somewhat subjective and difficult to document, leading to results that are often difficult to reproduce. The final problem is that available paleoseismic recurrence-interval estimates, which are matched explicitly in step (2), may no longer be matched after the moment balancing of step (3). With respect to segmentation, both WGCEP (2003) and WGCEP (2008) also included some form of an unsegmented model, but these did not generally match both the paleoseismic and slip-rate data either.

This paper presents a relatively objective and reproducible methodology that avoids assuming segmentation and is able to match both paleoseismic recurrence-interval data and slip-rate data simultaneously. While we use the southern San Andreas fault (SSAF) to exemplify the methodology, an important attribute is that it is extensible to a potentially complex network of faults; in this sense our work builds on that of Andrews and Schwerer (2000). This extensibility will allow the inclusion of multifault ruptures, the need for which was emphasized by WGCEP (2008). This methodology can also be used to quantify whether collecting additional paleoseismic data at a site might be useful or even to optimize the location of new sites. While this study shares some similarities to the so-called "stringing pearls" approach of Biasi and Weldon (2009), their study was aimed at determining the actual rupture history of the SSAF over the last 2000 years,

whereas we are interested in determining the long-term, average rate of events on the fault.

The General Solution

Our goal is to solve for the long-term rate of every possible earthquake rupture (above some threshold magnitude) on the fault or fault system. For simplicity, we restrict our attention here to earthquakes that rupture the entire seismogenic thickness of the fault (i.e., the entire down-dip width). Our first step is to divide the fault(s) into some large number (S) of subsections, as exemplified in the bottom image of Figure 1, and to define the total number of possible ruptures (R) as the entire set of contiguous subsection combinations. Again, our goal is to solve for the long-term rate of each of these possible ruptures by satisfying slip-rate and event-rate data, and perhaps other constraints, which we do by setting up a system of equations that can be solved using standard inverse theory.

Our first set of equations involves satisfying fault slip-rate estimates:

$$\sum_{r=1}^{R} D_{sr} f_r = v_s, \tag{1}$$

where v_s is the average long-term slip rate of the sth subsection, D_{sr} is the average slip in the rth rupture on the sth subsection (specified *a priori* as exemplified subsequently in this paper), and f_r is the rate or frequency of the rth rupture (to be solved for). This gives S equations for the R unknowns (assuming a slip-rate estimate is available for all subsections).

Our second set of equations involves satisfying any paleoseismically derived estimates of average event rates (the reciprocal of the mean recurrence interval) at points along the fault:

$$\sum_{r=1}^{R} \mathbf{G_{sr}} P_r^{\text{paleo}} f_r = f_s^{\text{paleo}}, \tag{2}$$

where $\mathbf{G_{sr}}$ is a matrix indicating whether the rth rupture involves the sth subsection (1 if so, 0 if not), P_r^{paleo} is the probability that the rth rupture would be seen in a paleoseismic trench (exemplified later in this paper), and f_s^{paleo} is the paleoseismically inferred event-rate estimate for that subsection.

The third set of equations applies to any *a priori* rupture rate estimates that might be available (e.g., the rate of Parkfield earthquakes should equal the historical rate of 1 approximately every 25 years; Bakun *et al.*, 2005):

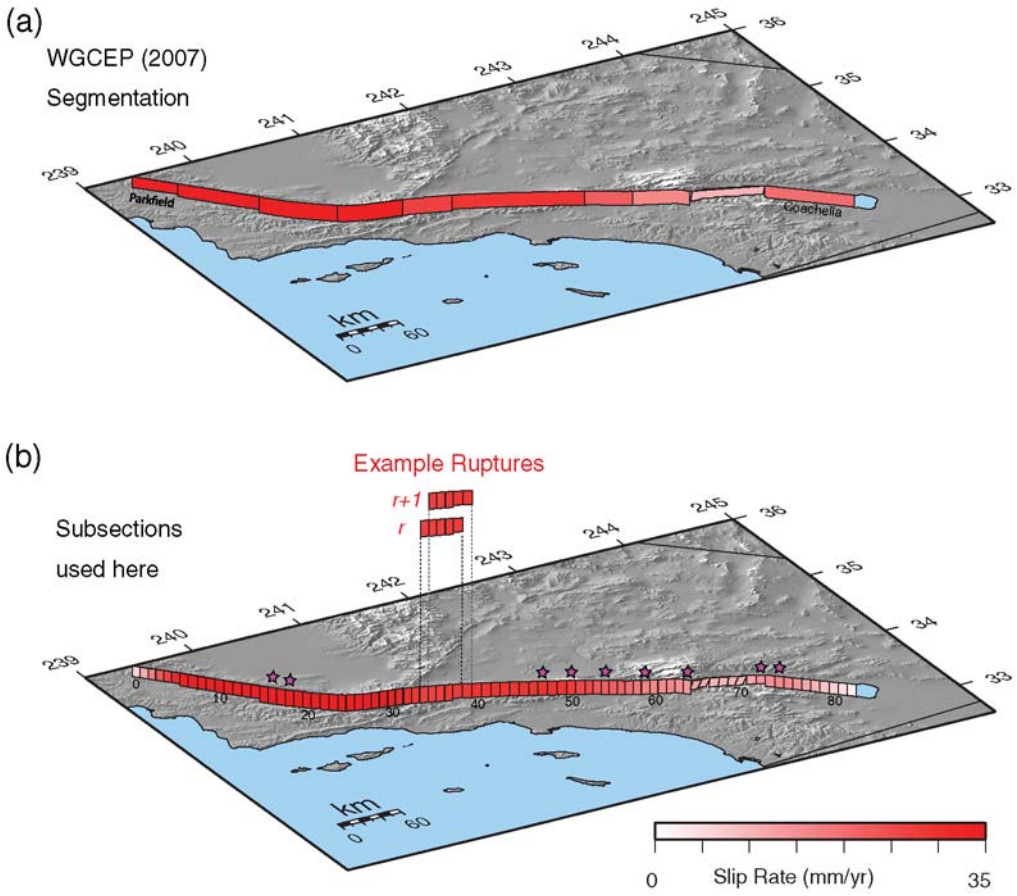

Figure 1. (a) Fault sectioning and segmentation of WGCEP (2008) and (b) the subsectioning applied in this paper. The numbers below some of the subsections in (b) correspond to the indexes used in subsequent figures, and the stars indicate locations where paleoseismic event-rate constraints exist (Table 4).

$$f_r = f_r^{a\ priori}. \tag{3}$$

Alternatively, we may want to stipulate that the total rate of events on some subsection be equal to an *a priori* estimate (e.g., that the total rate of all events involving a given Parkfield subsection equal the historical value of 1 approximately every 25 years), as in our fourth equation set:

$$\sum_{r=1}^{R} \mathbf{G_{sr}} f_r = f_s^{a\ priori}. \tag{4}$$

In order to further condition the inversion, we can add a smoothness constraint to the fifth equation set that stipulates the rate of earthquakes of a given size should not vary along the fault (unless the data described previously demand otherwise):

$$f_r - f_{r+1} = 0, \tag{5}$$

which we apply to all ruptures that are adjacent, maximally overlapping along the fault, and involving the same number of subsections (see the Example Ruptures in Fig. 1). The justification for this constraint might be physical (e.g., nature does not generally exhibit changes in the rate of similar-sized events along a fault) or practical (e.g., we do not want earthquake insurance premiums to reflect such rate variations unless data demand otherwise).

The final equation set involves constraining the entire set of earthquake rates to be consistent with some *a priori* magnitude–frequency distribution:

$$\sum_{r=1}^{R} M_r f_r = f_{m\pm\Delta m}^{a\ priori}, \tag{6}$$

where $f_{m\pm\Delta m}^{a\ priori}$ is the total rate of earthquakes in the range $m \pm \Delta m$ and M_r is a vector that states whether or not the rth rupture has a magnitude that is in this range. By spanning a range of discrete magnitudes, one can impose an entire magnitude–frequency distribution (although if one wants to solve for the best fitting parameters of a specific distribution, such as a Gutenberg–Richter distribution (Ishimoto and Iida, 1939; Gutenberg and Richter, 1944), it must be done iteratively as exemplified subsequently in our paper).

The preceding set of equations can easily be solved in the least-squares sense using standard linear inverse theory (e.g., Menke, 1989). Specifically, if we combine all available equations into one system as:

$$\boldsymbol{Xf} = \boldsymbol{d},$$

where $\boldsymbol{f}$ is a vector of rupture rates that we wish to solve for and $\boldsymbol{d}$ is a vector of data constraints, then the least-squares solution is simply that which minimizes the total squared prediction error (defined as the sum of the squares of the differences between the observed and predicted data):

$$E = \sum_i (d_i^{\text{obs}} - d_i^{\text{pre}})^2 = (\boldsymbol{d} - \boldsymbol{Xf})^T (\boldsymbol{d} - \boldsymbol{Xf}),$$

where i corresponds to the ith subsection or rupture (depending on the type of constraint). If we have uncertainty estimates for the data (σ_{d_i}), then we can solve for the weighted least-squares solution by minimizing

$$E = \sum_i \left[\frac{(d_i^{\text{obs}} - d_i^{\text{pre}})}{\sigma_{d_i}} \right]^2 = (\boldsymbol{d} - \boldsymbol{Xf})^T \boldsymbol{W} (\boldsymbol{d} - \boldsymbol{Xf}), \tag{7}$$

where $\boldsymbol{W}$ is a diagonal matrix of weights ($1/\sigma_{d_i}^2$). This weighted least-squares solution assumes the relative data uncertainties are adequately approximated by known uncorrelated Gaussian distributions.

Because earthquake rates cannot be negative, an important additional constraint is positivity:

$$f_r \geq 0.$$

While this is helpful in terms of further narrowing the solution space, it makes finding and understanding the inverse solution more difficult (e.g., singular value decomposition cannot be used). We use the nonnegative least-squares (NNLS) solution of Lawson and Hanson (1974). The weighted inversion is obtained by multiplying both sides of each equation by $1/\sigma_i$ before solving the NNLS problem. Note that the positivity constraint on f_r, and v_s and f_s^{paleo} for that matter, is an explicit violation of the presumed Gaussian statistics; we proceed nonetheless.

There may be a desire to force a better fit with respect to any one of the equation sets described thus far in this paper (or to give the various sets relative preferences). This can be accomplished by simply multiplying both sides of the equations for a given set by a relative weight. This allows the solution to be fine-tuned in order to balance the various constraints (which admittedly adds a degree of subjectivity, but at least these choices are easily documented and results are therefore reproducible).

Finally, to prevent the inversion from setting too many rupture rates to zero (as is exemplified subsequently here), it may be desirable to force final rates to be greater than some specified minimum values ($f_r \geq f_r^{\min}$). Putting these values into a vector $\boldsymbol{f}^{\min}$, we achieve this constraint by defining

$$\boldsymbol{f}' = \boldsymbol{f} - \boldsymbol{f}^{\min}$$

and

$$\boldsymbol{d}' = \boldsymbol{d} - \boldsymbol{Xf}^{\min},$$

solving

$$\boldsymbol{Xf}' = \boldsymbol{d}'$$

for $\boldsymbol{f}'$ using NNLS, and then obtaining the final solution as

$$\boldsymbol{f} = \boldsymbol{f}' + \boldsymbol{f}^{\min}.$$

Application to the Southern San Andreas Fault

Here we exemplify the methodology using the southern San Andreas fault. It is important to note that, although we believe the SSAF models presented here are at least as defensible as anything else published, a more thorough exploration of parameter sensitivity and propagation of epistemic uncertainties is warranted before making any formal conclusions or recommendations. The point here is to exemplify our relatively objective and reproducible methodology.

This implementation has been accomplished using code available from OpenSHA (Field *et al.*, 2003; see the Data and Resources section). Table 1 lists and describes the parameters that are adjustable in our implementation, which are subsequently discussed in the context of the solutions presented here. Each of these parameters represents an epistemic uncertainty, and again, it is beyond the scope of this paper to fully explore the influence of each (let alone the influence of other possible parameterizations).

Table 1
Parameters Used in OpenSHA Inversion Implementation for the Southern San Andreas Fault

Parameter Name	Preferred Value	Allowed Values	Description
maxSubsectionLength	7 (km)	1–25 (km)	Sets the maximum length of fault subsections, where the actual subsection length is determined by dividing the entire section length by the smallest whole number that produces subsection lengths less than or equal to the value specified by this parameter.
numSegForSmallestRups	2	1 or 2	The minimum number of subsections involved in any rupture.
deformationModel	D2.1	D2.1, D2.2, or D2.3	Specifies which of three southern San Andreas fault slip-rate models to use. See WGCEP (2008) for details.
moRateReduction	0.1	0–1	Specifies the amount of the subsection slip rates that is accounted for by earthquakes smaller than the full down-dip ruptures considered here; see WGCEP (2008) for more discussion.
transitionAseisAtEnds	Yes	Yes or No	Determines whether subsection aseismicity values are linearly transitioned in the sections at the ends of the fault (Parkfield and Coachella).
transitionSlipRateAtEnds	Yes	Yes or No	Determines whether subsection slip rates are linearly transitioned in the sections at the ends of the fault (Parkfield and Coachella), in order to transition into the creeping sections.
slipRateSmoothing	5	Positive whole number	If greater than 1, this applies a boxcar smoothing to all the subsection slip rates, where the value given here is the width of the boxcar in terms of the number of subsections. For example, if *slipRate Smoothing*, the slip rate of a given subsection is the average of itself and its two neighbors on each side.
slipModelType	Tapered Ends	WGCEP-2002, Uniform/Boxcar, or Tapered Ends	Specifies how the average slip varies among the subsections involved in a given rupture. Uniform/Boxcar means the slip in all subsections is the same. The WGCEP-2002 option means the slip in each subsection is proportional to the subsection slip rate. The Tapered Ends option means slip rate decreases toward the ends of the rupture, following the $\sin(x)^{0.5}$ function. See WGCEP (2008) for more details.
magAreaRel	Hanks & Bakun (2008)	Ellsworth-A, Ellsworth-B, Hanks & Bakun (2008), or Somerville (2006)	This specifies the magnitude–area relationship used to compute the magnitude (and average slip) from the rupture area. Ellsworth-A and Ellsworth-B are from equation (3.5a) and (3.5b), respectively, of WGCEP (2003). The others are as referenced.
applyProbVisible	Yes	Yes or No	When set to "yes," the inversion accounts for the fact that not all ruptures will be seen in a paleoseismic trench.
wtedInversion	Yes	Yes or No	When set to "yes," the data uncertainties are used in a weighted least-squares inversion (via equation 7).
minRupRate	1×10^{-6}	0 to ∞	This sets a minimum rate for all ruptures.
relativeSegRateWt	1	0 to ∞	This sets the weight of equation set 2 relative to equation set 1.
relative_aPrioriRupWt	100	0 to ∞	This sets the weight of equation set (3) relative to equation set (1).
relative_aPrioriSegRateWt	100	0 to ∞	This sets the weight of equation set (4) relative to equation set (1).
relative_smoothnessWt	10	0 to ∞	This sets the weight of equation set (5) relative to equation set (1).
relativeGR_constraintWt	0.0	0 to ∞	This sets the weight of equation set (6) relative to equation set (1).
grConstraintBvalue	1	−2 to 2	If *relativeGR_constraintWt* is not zero, this sets the *b* value of the Gutenberg–Richter distribution.
grRateAtM6.5	0.011	0 to ∞	If *relativeGR_constraintWt* is not zero, this sets the Gutenberg–Richter rate of events at the magnitude 6.5 bin (between 6.45 and 6.55).

Adopting the parlance and data model of WGCEP (2008), we start with a fault-section dataset for the SSAF, which gives the following set of geometrical and kinematic parameters for each fault section: (1) name, (2) fault trace, (3) average dip, (4) average upper and lower seismogenic depth, (5) average long-term slip rate, (6) average rake, and (7) average aseismic slip factor (defined as the fraction of moment released by creep between the upper and lower seismogenic depths). Figure 1a and Table 2 contain the fault-section dataset used here for the SSAF, which comes from WGCEP (2008). The slip rates listed are for one of the three deformation models developed by WGCEP (2008), as chosen by the *deformationModel* parameter in Table 1.

Note that this fault sectioning is for descriptive purposes only and does not necessarily imply any rupture segmentation. In fact, distinct fault sections were defined only where one or more of the associated parameters changes significantly along the fault, meaning the sections can be arbitrarily long if the parameters do not change. Therefore, we need to subdivide these sections into small enough lengths that the model is effectively unsegmented. As with previous WGCEPs, we restrict ourselves to solving for the rate of earthquakes that rupture the entire seismogenic thickness (~14 km for the SSAF), so the smallest events we are considering are about 14 km × 14 km. To enable these ruptures to occur anywhere along the fault (at some reasonable level of discretization), we subdivide each fault section into subsections that are about 7 km in length (half the average down-dip width) using the *maxSubsectionLength* parameter in Table 1. This leads to the 83 subsections listed in Table 2, producing an effectively unsegmented model compared to the 11 segments applied by WGCEP (2008).

We now define the set of possible ruptures as all those involving two or more contiguous subsections, where the lower limit of two is chosen (via the *numSegForSmallestRups* parameter in Table 1) so the smallest ruptures have approximately square dimensions with respect to the seismogenic thickness (and avoiding unrealistic aspect ratios where the down-dip width would be about two times the rupture length). Given that there are no branches in our fault model, the total number of ruptures is 3,403 (two of these are shown as Example Ruptures in Fig. 1). This level of discretization represents a balance between our goal of relaxing segmentation (which argues for a greater number of shorter subsections) and the computational demands of the problem in terms of memory and the central processing unit.

The mean magnitude for each earthquake rupture is computed using a magnitude–area relationship (Table 1); in our example solutions here, we use the relationship of Hanks and Bakun (2008). Following WGCEP (2008), the aseismicity parameters are applied as a reduction of seismogenic area in computing these magnitudes. For the fault sections at the ends of the fault (at Parkfield and Coachella), we apply a linear transition of aseismicity values over the subsections while preserving the original, average value for the entire section (via the *transitionAseisAtEnds* parameter in Table 1, leading to the final values given in Table 2). This is done to avoid abrupt changes in aseismicity along the fault, although results are not heavily influenced by the application of this modification. The mean magnitudes for each rupture are rounded to the nearest tenth of a unit; and, following WGCEP (2008), an aleatory variability over magnitude is given for each rupture as listed in Table 3 (a Gaussian distribution with sigma = 0.12, truncated at $\pm\sigma$, and discretized at 0.1 values).

To avoid producing a very high rate of smaller events at the ends of the fault, we also linearly transition the slip rates to zero over the Parkfield and Coachella subsections as they approach the creeping sections to the north and south, respectively (accomplished via the *transitionSlipRateAtEnds* parameter in Table 1). Similarly, to avoid abrupt changes in fault slip rates at the fault-section boundaries, which would introduce artificial rupture segmentation, we also smooth the subsection slip rates along the fault using a 5-point boxcar function (via the *slipRateSmoothing* parameter in Table 1). Both of these adjustments produce the modified slip rate values listed in Table 2 (and shown in Fig. 1b). Following WGCEP (2008), these slip rates are further reduced before application in equation set (1) according to the value of *moRateReduction* in Table 1 (which accounts for the fraction of moment rate released by events smaller than the full seismogenic ruptures modeled here).

Solving equation set (1) requires specifying the slip on a given subsection for a given rupture (D_{sr}). First, the average slip for each rupture is computed from magnitude, area, and an assumed shear rigidity of 3×10^1 N m using the standard moment-magnitude relationship (Hanks and Kanamori, 1979). This average slip is then partitioned over the subsections according to which type of slip model is chosen (via the *slipModelType* parameter described in Table 1). Following WGCEP (2008), which comes from Weldon *et al.* (2008), we use the tapered ends model for the examples here, where slip gets lower toward the ends of the rupture.

The SSAF paleoseismic event-rate data available for use in equation set (2) are listed in Table 4 (from Parsons, 2007) and shown with stars in Figure 1. For P_r^{paleo} in equation set (2), which gives the probability that a rupture will be seen in a paleoseismic trench, we use equation (4) of Youngs *et al.* (2003), which originally comes from Wells and Coppersmith (1993):

$$P_r^{\text{paleo}} = \frac{e^{M \times 2.053 - 12.51}}{1 + e^{M \times 2.053 - 12.51}},$$

where M is the magnitude of the rupture. This produces probabilities of 0.45, 0.87, and 0.98 for magnitudes 6, 7, and 8, respectively.

The only *a priori* rate constraints applied in equation sets (3) and (4) are to control the behavior of Parkfield earthquakes (otherwise the rate of this event is too low, and the rate of smaller events in this fault section are too high). We first attempted to simply set the rate of Parkfield earthquakes

Table 2

Data for the Southern San Andreas Fault Sections* and Subsections Used for This Study

Fault-Section Data							Subsection Data			
Name	Trace (Latitude, Longitude)	Down-Dip Width (km)	Length (km)	Average Slip Rate (mm/yr)	Slip-Rate Standard Deviation	Aseismic Slip Factor	Index	Length (km)	Modified Slip Rate (mm/yr)	Aseismic Slip Factor
Parkfield	35.75198, −120.30005	10.2	36.4	34	2.5	0.79	0	6.07	5.67	0.94
	36.00265, −120.56089						1	6.07	11.33	0.88
							2	6.07	17.00	0.82
							3	6.07	22.67	0.76
							4	6.07	27.20	0.70
							5	6.07	30.60	0.64
Cholame	35.31417, −119.86595	12.0	62.5	34	2.5	0.00	6	6.95	32.87	0.00
	35.41391, −119.97030						7	6.95	34.00	0.00
	35.53331, −120.08675						8	6.95	34.00	0.00
	35.75198, −120.30005						9	6.95	34.00	0.00
							10	6.95	34.00	0.00
							11	6.95	34.00	0.00
							12	6.95	34.00	0.00
							13	6.95	34.00	0.00
							14	6.95	34.00	0.00
Carrizo	35.31420, −119.86590	15.1	59.0	34	1.5	0.00	15	6.56	34.00	0.00
	35.16070, −119.70680						16	6.56	34.00	0.00
	35.04750, −119.55830						17	6.56	34.00	0.00
	34.98780, −119.47110						18	6.56	34.00	0.00
	34.94410, −119.40290						19	6.56	34.00	0.00
							20	6.56	34.00	0.00
							21	6.56	34.00	0.00
							22	6.56	34.00	0.00
							23	6.56	34.00	0.00
Big Bend	34.94406, −119.40286	15.1	49.7	34	1.5	0.00	24	6.22	34.00	0.00
	34.91571, −119.36286						25	6.22	34.00	0.00
	34.86390, −119.21000						26	6.22	34.00	0.00
	34.82896, −119.03009						27	6.22	34.00	0.00
	34.80760, −118.89012						28	6.22	34.00	0.00
							29	6.22	34.00	0.00
							30	6.22	32.60	0.00
							31	6.22	31.20	0.00
Mojave N	34.80760, −118.89012	15.1	36.9	27	3.5	0.00	32	6.14	29.80	0.00
	34.80722, −118.88764						33	6.14	28.40	0.00
	34.77325, −118.76731						34	6.14	27.00	0.00
	34.69849, −118.50895						35	6.14	27.00	0.00
							36	6.14	27.40	0.00
							37	6.14	27.80	0.00

(*continued*)

Table 2 (*Continued*)

Fault-Section Data							Subsection Data			
Name	Trace (Latitude, Longitude)	Down-Dip Width (km)	Length (km)	Average Slip Rate (mm/yr)	Slip-Rate Standard Deviation	Aseismic Slip Factor	Index	Length (km)	Modified Slip Rate (mm/yr)	Aseismic Slip Factor
Mohave S	34.69849, −118.50895	13.1	97.6	29	3.5	0.00	38	6.97	28.20	0.00
	34.54785, −118.10393						39	6.97	28.60	0.00
	34.40293, −117.75358						40	6.97	29.00	0.00
	34.31630, −117.54900						41	6.97	29.00	0.00
							42	6.97	29.00	0.00
							43	6.97	29.00	0.00
							44	6.97	29.00	0.00
							45	6.97	29.00	0.00
							46	6.97	29.00	0.00
							47	6.97	29.00	0.00
							48	6.97	29.00	0.00
							49	6.97	29.00	0.00
							50	6.97	27.60	0.00
							51	6.97	26.20	0.00
San Bernardino N	34.31630, −117.54900	12.8	35.3	22	3.0	0.00	52	5.88	24.80	0.00
	34.27090, −117.45100						53	5.88	23.40	0.00
	34.23284, −117.38869						54	5.88	22.00	0.00
	34.17314, −117.27416						55	5.88	22.00	0.00
	34.15003, −117.22202						56	5.88	20.80	0.00
							57	5.88	19.60	0.00
San Bernardino S	34.15003, −117.22202	12.8	43.4	16	3.0	0.00	58	6.20	18.40	0.00
	34.09280, −117.06767						59	6.20	17.20	0.00
	34.07377, −117.01390						60	6.20	16.00	0.00
	34.03384, −116.90235						61	6.20	16.00	0.00
	34.01135, −116.87354						62	6.20	16.00	0.00
	33.95911, −116.81979						63	6.20	14.80	0.00
							64	6.20	13.60	0.00
San Gorgonio Pass–Garnet Hill	33.78825, −116.24629	15.1	55.9	10	3.0	0.00	65	6.98	12.40	0.00
	33.84852, −116.38300						66	6.98	11.20	0.00
	33.84812, −116.42653						67	6.98	10.00	0.00
	33.88466, −116.51689						68	6.98	10.00	0.00
	33.90702, −116.58485						69	6.98	10.00	0.00
	33.91757, −116.62387						70	6.98	10.00	0.00
	33.94416, −116.68581						71	6.98	12.00	0.00
	33.93741, −116.77859						72	6.98	13.60	0.00
	33.95316, −116.80139									

(*continued*)

Table 2 (*Continued*)

Fault-Section Data							Subsection Data			
Name	Trace (Latitude, Longitude)	Down-Dip Width (km)	Length (km)	Average Slip Rate (mm/yr)	Slip-Rate Standard Deviation	Aseismic Slip Factor	Index	Length (km)	Modified Slip Rate (mm/yr)	Aseismic Slip Factor
Coachella	33.78825, −116.24629	11.1	69.4	20	3.0	0.10	73	6.94	14.80	0.02
	33.35009, −115.71192						74	6.94	15.60	0.04
							75	6.94	16.00	0.05
							76	6.94	14.00	0.07
							77	6.94	12.00	0.09
							78	6.94	10.00	0.11
							79	6.94	8.00	0.13
							80	6.94	6.00	0.15
							81	6.94	4.00	0.16
							82	6.94	2.00	0.18

*From WGCEP (2008). Not listed are the dips for each fault section, which are 90 degrees for all but San Gorgonio Pass–Garnet Hill, which has a dip of 58 degrees.

Table 3
Distribution of Magnitudes Assigned to Each Rupture*

Magnitude	Probability
mean − 0.2	0.09
mean − 0.1	0.24
mean	0.34
mean + 0.1	0.24
mean + 0.2	0.09

*The means are given by the chosen magnitude–area relationship. The probabilities are taken from a Gaussian distribution with sigma = 0.12, truncated at $\pm 2\sigma$ and discretized at 0.1 values.

to be the historically observed value of 0.04 (once every ~25 years; Bakun *et al.*, 2005). However, doing so led the total rate of one Parkfield subsection to be too high (an event every ~13 years) due to the influence of other ruptures that involve this subsection. Alternatively, we tried using equation set (4) to make the total rate of each Parkfield subsection equal to 0.04, but this led to the Parkfield rupture itself being too rare. As a compromise, in the results presented here, we ended up applying this constraint to both the Parkfield rupture and to each of the Parkfield subsections. Again, the point here is not to defend these specific decisions but rather to exemplify how such issues can be addressed in our framework.

The *minRupRate* parameter in Table 1 forces the rate of all ruptures to be greater than or equal to this value as described in The General Solution section. Several other parameters in Table 1 govern how the various equations in the inversion are weighted. The *wtedInversion* parameter simply tells whether to apply the slip-rate and event-rate uncertainties (listed in Tables 2 and 4, respectively) in a weighted-inversion minimization of equation (7). The *relativeSegRateWt*, *relative_aPrioriRupWt*, *relative_aPrioriSegRateWt*, and *relative_smoothnessWt* give the weights for equation sets (2), (3), (4), and (5), respectively, all of which are relative to equation set (1). As previously stated, application of these weights simply involves multiplying both sides of the equations within each set by the associated value before performing the inversion. The smoothness constraint represented by equation set (5) is applied here to ruptures that are both adjacent (in terms of index) and involve the same number of subsections.

Finally, the *relativeGR_constraintWt* parameter in Table 1 specifies the extent to which the solution is forced to conform to a Gutenberg–Richter distribution via equation set (6), where we use $\Delta m = 0.05$ (bin widths of 0.1 magnitude units). The aleatory variability is ignored in assigning each rupture to a magnitude bin (only the mean magnitude is considered). The *b* value of this distribution is set by the *grConstraintBvalue* parameter, and the *grRateAtM6.5* parameter is used to set the rate of events in the magnitude 6.5 bin (which establishes the *a* value, from which the rate of events in all other bins in equation set (6) can be computed using the Gutenberg–Richter relationship). The value of this latter parameter is found iteratively by searching for that which minimizes the total prediction error.

Results

Results for the inversion using the preferred values in Table 1 are shown in Figure 2. Figure 2a shows the fit to slip-rate data, Figure 2b shows the fit to paleoseismic event-rate data, Figure 2c shows the total magnitude-frequency distribution for the solution, and Figure 2d plots the spatial distribution of all ruptures that have a final rate greater than the *minRupRate* value in Table 1. We quantify the goodness of fit to the slip-rate data with the following normalized slip-rate residual:

$$\sqrt{\sum\left[\frac{(v_i^{\mathrm{obs}} - v_i^{\mathrm{pre}})}{\sigma_{v_i}}\right]^2}.$$

For the results in Figure 2a, this residual is 0.11, and the equivalent event-rate residual for results in Figure 2b is 0.34. The Parkfield earthquake, which has a mean magnitude of 5.9, has a final predicted recurrence interval of 37 years, with the lowest interval for any one of its subsections being

Table 4
Paleoseismic Data for the Southern San Andreas Fault

Site	Latitude (°)	Longitude (°)	Subsection Index*	Average Rate†	Rate Sigma (Standard Deviation)	2.5% Percentile‡	97.5% Percentile‡
Bidart	35.2328	−119.7872	16	0.005882	0.003529	0.001282	0.020000
Combined Carrizo	35.1540	−119.7000	18	0.003571	0.001924	0.001235	0.008333
Pallett Creek	34.4556	−117.8870	47	0.007353	0.002495	0.003534	0.013514
Wrightwood	34.3697	−117.6680	50	0.010204	0.005476	0.005714	0.016667
Pitman Canyon	34.2544	−117.4340	54	0.004545	0.002679	0.002273	0.012500
Plunge Creek	34.1158	−117.1370	59	0.002083	0.004005	0.000676	0.012500
Burro Flats	33.9730	−116.8170	64	0.002381	0.002494	0.002174	0.011111
1000 Palms	33.8200	−116.3010	72	0.002941	0.002108	0.001075	0.010000
Indio	33.7414	−116.1870	74	0.003125	0.002328	0.000855	0.011111

*The Subsection Index gives the corresponding subsection from Table 2.

†Average event rate = one over the mean recurrence interval, assuming the southern San Andreas fault exhibits a Poisson distribution of interevent times (see Appendix C of WGCEP (2008) or Parsons (2007) for details).

‡The 2.5 and 97.5 percentiles represent the 95-percent confidence bounds.

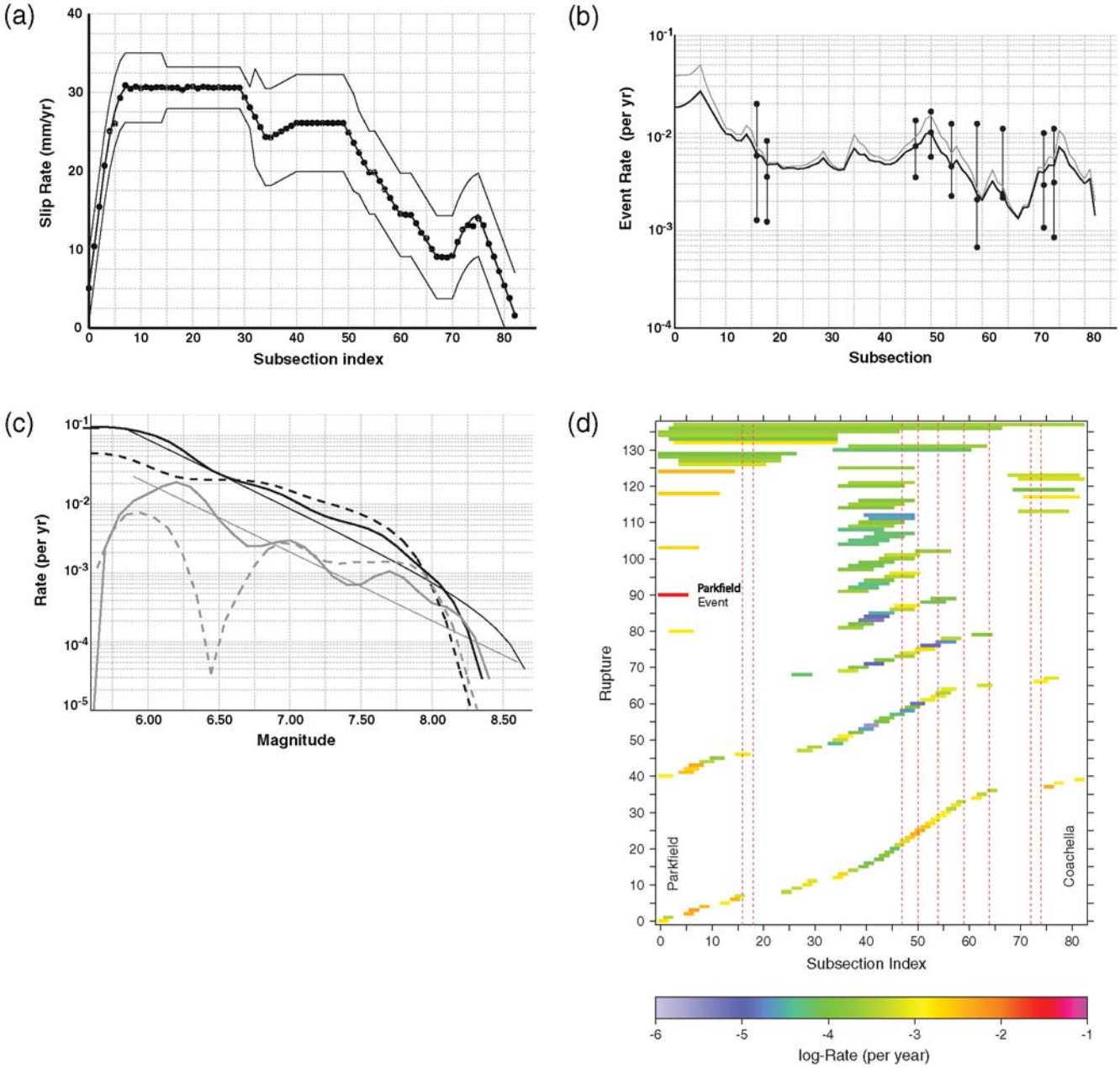

Figure 2. Inversion results. (a) The fit to slip-rate data: thick black line, mean slip rate for each subsection; thinner black lines, 95% confidence bounds; black dots, final model slip rates for the solution based on the preferred parameter values in Table 1. Subsection indices increase from Parkfield at the north to Coachella at the south. (b) The fit to paleoseismic event-rate data: thick black line, final model event rates at each subsection for the solution based on the preferred parameter values in Table 1; black dots, mean event-rate constraints and corresponding 95% confidence bounds from Table 4. The thick black line includes the probability that each event is paleoseismically observable (the P_r^{paleo} term in equation set 2), whereas the thinner gray line gives the total rate for comparison. (c) The total magnitude-frequency distribution for the solution: thicker black and gray lines, the model-predicted incremental and cumulative magnitude-frequency distributions, respectively, for the solution based on the preferred parameter values from Table 1. The thinner lines show results for a pure Gutenberg–Richter distribution for comparison, where the *a* value was chosen to match the model-predicted cumulative rate at magnitude 6.5, and the upper magnitude was chosen to match the overall moment-rate of the model. The black and gray dashed lines are the incremental and cumulative distributions from WGCEP (2008), averaged over all logic-tree branches. (d) Rate and spatial distribution of each rupture that has a rate greater than *minRupRate*, for the solution based on preferred parameter values in Table 1. The *x* axis gives the index of the subsection, with Parkfield to the left and Coachella to the right. Dashed lines give the locations where the paleoseismic event-rate constraints exist.

20 years and the average over all six subsections being 24 years. The value of 100 applied for the *relative_aPrioriRupWt* and *relative_aPrioriSegRateWt* parameters in Table 1 were found to adequately balance the tradeoff between the Parkfield event and subsection rates (see the Application to the Southern San Andreas Fault section).

We originally set the *minRupRate* parameter to zero, but the inversion ended up giving a nonzero rate to only 148 out

of the 3403 possible ruptures (with all other parameters set as in Table 1). To avoid saying any rupture cannot happen, we gradually increased the value of the *minRupRate* parameter until it just started influencing the slip-rate and event-rate residuals. This modification forces every event to have a non-zero rate, but only 138 out of the 3403 ruptures have rates greater than the minimum value (shown in Fig. 2d). For the smoothness constraints of equation set (5), we increased the value of the *relative_smoothnessWt* parameter until it, too, just began influencing the slip-rate and event-rate residuals.

Note that, for the results in Figure 2, no Gutenberg–Richter constraint was applied. The resultant magnitude–frequency distribution (Fig. 2c) implies slightly elevated rates at the largest magnitudes, relative to a Gutenberg–Richter, consistent with a more characteristic magnitude–frequency distribution (e.g., Wesnousky *et al.*, 1983; Schwartz and Coppersmith, 1984; Stirling *et al.*, 1996). This solution does not, however, have as elevated a rate of large earthquakes as the original characteristic earthquake hypothesis, which (as originally formulated) postulated rates of large earthquakes an order of magnitude higher than would be predicted by a Gutenberg–Richter extrapolation from small magnitudes. Figure 3 shows an equivalent set of results wherein a Gutenberg–Richter distribution with a *b* value of 1.0 has been

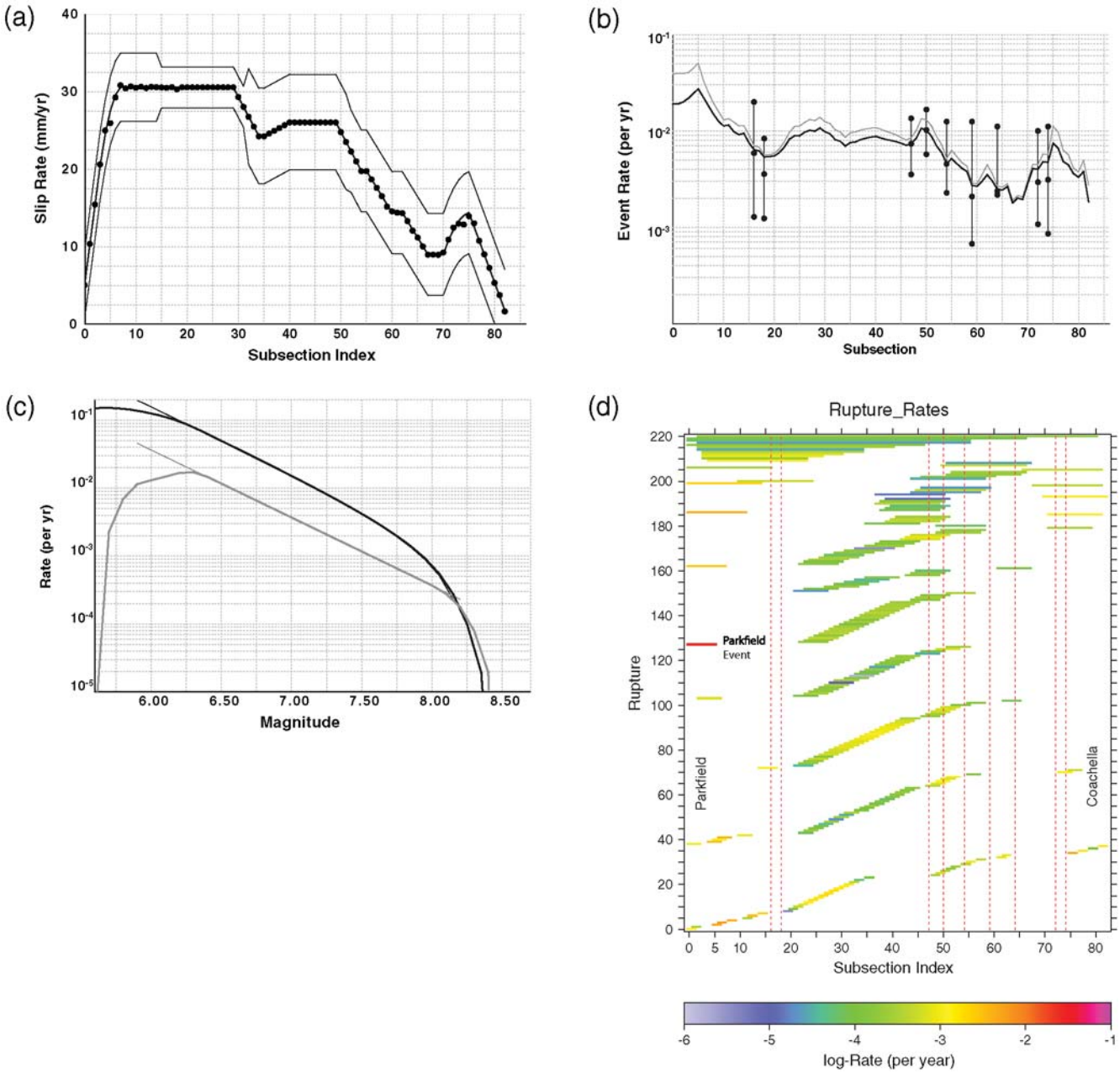

Figure 3. (a–d). Same as Figure 2a–d except that a Gutenberg–Richter constraint has been applied as described in the text (*relativeGR_constraintWt* $= 1 \times 10^6$, *gr*Constraint*B*value $= 1.0$, and *gr*Rate*AtM*6.5 $= 0.011$).

enforced via equation set (6) (by setting *relativeGR_constraintWt* $= 1 \times 10^6$ and *gr*Constraint*B*value $= 1.0$). This constraint was applied between magnitudes 6.2 and 8.2, and the value of the *grRateAtM6.5* parameter was found via a grid search that minimized the total prediction error. The slip-rate and event-rate residuals for this case are 0.12 and 0.43, respectively, so only the latter is slightly greater than for the unconstrained case in Figure 2 (where values are 0.11 and 0.34, respectively). Therefore, it appears that both a somewhat characteristic distribution and a Gutenberg–Richter distribution are viable for the SSAF.

Interestingly, applying a Gutenberg–Richter constraint with a *b* value of 0.0 (a uniform distribution), as applied by WGCEP (2008) for their unsegmented model option, produces slip-rate and event-rate residuals of 1.4 and 0.93, respectively. Thus, it appears that a *b* value of 0.0 is not consistent with the slip-rate and event-rate data. Figure 2c also includes the magnitude–frequency distribution obtained by the WGCEP (2008) for the SSAF (averaged over all logic-tree branches), which is appreciably different from the results obtained here.

Discussion

Our intent here has been to introduce and exemplify a relatively objective and reproducible methodology for determining the long-term rate of events on a fault or fault system. There are several aspects of the example presented here that are tempting to present and discuss, including the magnitude–frequency distributions at points along the fault, the total rate at which subsection boundaries constitute endpoints of ruptures (getting to the question of fault segmentation), and the degree that each rupture contributes to the slip rate along the fault. Perhaps most provocatively, our results contribute to a growing body of evidence that a Gutenberg–Richter distribution might apply to the San Andreas fault (e.g., Jackson and Kagan, 2006; Page *et al.*, 2009; Parsons and Geist, 2009). As shown in Figure 2c, our results are certainly different from the average magnitude–frequency distribution assigned to the SSAF by WGCEP (2008).

However, as stated at the outset of this paper, several items need to be examined further before drawing strong conclusions. One is the nature of the solution space for a given set of parameter values (like for the results shown in Fig. 2), especially because the vast majority of ruptures have final rates that are equal to the minimum value. We believe our problem is over determined, or at least mixed determined, especially given the smoothness constraint of equation set (5). The solution should therefore be well constrained or unique. However, the question remains as to the range of results represented by other solutions that, while not the best fit, nevertheless have an acceptable fit. As the reader can verify from Figure 1a,b, the NNLS solution overfits the data (i.e., the residuals are much smaller than the data errors). Because the NNLS algorithm does not allow us to explore alternative models for a given set of parameters, we plan to explore use of a simulated annealing algorithm (Kirkpatrick *et al.*, 1983) or other approaches in the future. Simulated annealing can generate multiple solutions to this nonlinear inverse problem, thus allowing us to probe the solution space of the model. This will be very important for identifying alternative models for a given set of parameters, which would represent epistemic uncertainties that could be used to populate a logic tree. This will also allow us address the tendency for NNLS solutions to force most values to be zero or the minimum allowed.

A second issue that needs to be explored before drawing strong conclusions is the sensitivity of results given reasonable alternative values for the parameters in Table 1 (also representing epistemic uncertainties). The difference between the inversion solutions with and without the *G-R* constraint demonstrates that alternative solutions could be quite different with regard to individual rupture rates (see Fig. 2d and Fig. 3d). Which parameters have the strongest effect and what properties of the solution are stable with respect to the inversion parameters are important subjects of future work.

A third question is the effect of our implementation of the slip-rate constraint, which is applied to every subsection. An alternative implementation would apply these constraints only at those points where the original slip-rate data were measured (perhaps with a smoothness constraint forcing final slip rates to change gradually along the fault, at least where there are no expected changes due to fault branching). Our application of the slip-rate constraint to every subsection, with an unmodified uncertainty estimate, probably gives this data too much weight in the inversion. Because our solutions fit the slip-rate and paleoseismic event-rate data fairly well, a fourth question deals with the range of models that would be obtained by sampling these data via Monte Carlo methods from the original probability distributions (rather than using mean values).

Other issues that warrant resolution before drawing definitive conclusions include: whether down-dip width is really constant over the magnitudes we have considered (e.g., King and Wesnousky, 2007); the validity of the Poisson assumption made in determining the paleoseismic recurrence intervals used here (Table 4 and Parsons, 2007); and the influence of more recent SSAF data that have been collected but not yet compiled in a usable form. A final issue is that we have ignored any ruptures that involve neighboring faults (e.g., ruptures that jump from the SSAF onto the San Jacinto or Cucamonga faults or ruptures that extend beyond the ends of the SSAF).

The fault-jumping issue brings us to reiterate the fact that our methodology is extensible to an entire fault system, such as the network of known California faults. As such, this represents an extension of the approach outlined by Andrews and Schwerer (2000) but where we have relaxed segmentation assumptions and have added equation sets (2)–(5). Applying our methodology to a fault system raises the question of how to account for the fact that multifault rupture

probabilities will depend on the separation between faults. However, even defining a binary distribution (e.g., allowing faults closer than 5 km to rupture together as if they were contiguous and not allowing faults at a greater distance to rupture together) would be better than the present approach of excluding multifault ruptures entirely (e.g., WGCEP, 2008).

Applying our methodology to an entire fault system will raise even greater issues with respect to solution uniqueness, especially because most faults have little or no paleoseismic event-rate constraints. One intriguing approach to addressing this problem is to use the rate of microseismicity near a fault to constrain the rate at which large events nucleate on the fault in that vicinity (by extrapolating an assumed magnitude–frequency distribution). Of course this inverse problem will become quite large, and it remains to be seen whether computational resources are available for solving it.

One constraint we have seemingly excluded here is the paleoseismically inferred estimates of slip in previous events. We have done so because these data are relatively sparse, the length of ruptures they are associated with are usually unknown, and the degree to which they represent the average slip for the event has considerable uncertainty. Most importantly, however, in many cases these data have already been used to help determine the slip rates we are using, so they are not independent constraints. It will be important that future studies consider the use of all such data more carefully.

Finally, the methodology presented here can be used to quantify the potential benefits of future paleoseismic studies, either by adding fictitious constraints in equation set (2) in order to test the potential impact or via a more sophisticated site optimization aimed at addressing specific questions (such as whether a fault is more characteristic or Gutenberg–Richter). Web-based applications could be deployed for this purpose if there is demand from the community.

Data and Resources

All data used in this paper came from published sources listed in the references. The OpenSHA code (Field *et al.*, 2003) is available from www.OpenSHA.org. Some plots were made using the Generic Mapping Tools version 3.4.5 (www.soest.hawaii.edu/gmt).

Acknowledgments

Thomas Parsons and Andrew Michael kindly provided constructive U.S. Geological Survey internal reviews. Mark Stirling, Ray Weldon, Russell Robinson, Karen Felzer, Kelvin Berryman, and one anonymous individual provided very useful and influential reviews for BSSA.

References

Andrews, D. J., and E. Schwerer (2000). Probability of rupture of multiple fault segments, *Bull. Seismol. Soc. Am.* **90,** 1498–1506.

Bakun, W. H., B. Aagaard, B. Dost, W. L. Ellsworth, J. L. Hardebeck, R. A. Harris, C. Ji, M. J. S. Johnston, J. Langbein, J. J. Lienkaemper, A. J. Michael, J. R. Murray, R. M. Nadeau, P. A. Reasenberg, M. S. Reichle, E. A. Roeloffs, A. Shakal, R. W. Simpson, and F. Waldhauser (2005). Implications for prediction and hazard assessment from the 2004 Parkfield earthquake, *Nature* **437,** 969–974, doi 10.1038/nature04067.

Biasi, G. P., and R. J. Weldon (2009). San Andreas fault rupture scenarios from multiple paleoseismic records: Stringing pearls, *Bull. Seismol. Soc. Am.* **99,** 471–498.

Field, E. H., T. H. Jordan, and C. A. Cornell (2003). OpenSHA: A developing community-modeling environment for seismic hazard analysis, *Seismol. Res. Lett.* **74,** 406–419.

Gutenberg, B., and C. Richter (1944). Frequency of earthquakes in California, *Bull. Seismol. Soc. Am.* **34,** 185–188.

Hanks, T. C., and W. H. Bakun (2008). M- log A observations for recent large earthquakes, *Bull. Seismol. Soc. Am.* **98,** 490–494.

Hanks, T. C., and H. Kanamori (1979). A moment magnitude scale, *J. Geophys, Res.* **84,** 2348–2350.

Ishimoto, M., and K. Iida (1939). Observations sur les seismes enregistres par le microseimographe construit dernierement, *Bull. Earthq. Res. Inst. Univ. Tokyo* **17,** 443–478 (in Japanese with French abstract).

Jackson, D. D., and Y. K. Kagan (2006). The 2004 Parkfield earthquake, the 1985 prediction, and characteristic earthquakes: Lessons for the future, *Bull. Seismol. Soc. Am.* **96,** S397–S409.

King, G. C. P., and S. G. Wesnousky (2007). Scaling of fault parameters for continental strike-slip earthquakes, *Bull. Seismol. Soc. Am.* **97,** 1833–1840, doi 10.1785/0120070048.

Kirkpatrick, S., C. D. Gelatt, and M. P. Vecchi (1983). Optimization by simulated annealing, *Science* **220,** 671–680.

Lawson, C. L., and D. J. Hanson (1974). *Solving Least Squares Problems*. Prentice-Hall, Englewood Cliffs, New Jersey, 340 pp.

Menke, W. (1989). *Geophysical Data Analysis: Discrete Inverse Theory*, Academic Press, Inc., San Diego, California, 289 pp.

Page, M. T., K. Felzer, R. J. Weldon, and G. Biasi (2009). The magnitude-frequency distribution on the Southern San Andreas fault: Reconciling instrumental, historic, and paleoseismic catalogs (abstract), *Seismol. Res. Lett.* **80,**, 325.

Parsons, T. (2007). Monte Carlo method for determining earthquake recurrence parameters from short paleoseismic catalogs: Example calculations for California, *J. Geophys. Res.* **113,** no. B03302, doi 10.1029/2007JB004998.

Parsons, T., and E. L. Geist (2009). Is there a basis for preferring characteristic earthquakes over a Gutenberg–Richter distribution in probabilistic earthquake forecasting?, *Bull. Seismol. Soc. Am.* **99,** 2012–2019.

Schwartz, D. P., and K. J. Coppersmith (1984). Fault behavior and characteristic earthquakes: Examples from the Wasatch and San Andreas fault zones, *J. Geophys. Res.* **89,** 5681–5698.

Somerville, P. (2006). Review of magnitude-area scaling of crustal earthquakes, *Report to WGCEP*, URS Corp., Pasadena, 22 pp.

Stirling, M. W., S. G. Wesnousky, and K. Shimazaki (1996). Fault trace complexity, cumulative slip, and the shape of the magnitude-frequency distribution for strike-slip faults: A global survey, *J. Geophys. Res.* **124,** 833–868.

Weldon, R. J., II, G. P. Biasi, C. J. Wills, and T. E. Dawson (2008). Overview of the southern San Andreas fault model; Appendix E in The Uniform California Earthquake Rupture Forecast, version 2 (UCERF 2), *U.S. Geol. Surv. Open-File Rept. 2007-1437-E, and California Geol. Surv. Special Rept. 203-E*, 53 pp., available at http://pubs.usgs.gov/of/2007/1437/e/.

Wells, D. L., and K. J. Coppersmith (1993). Likelihood of surface rupture as a function of magnitude, *Seismol. Res. Lett.* **64,** 54.

Wesnousky, S. G., C. H. Scholz, K. Shimazaki, and T. Matsuda (1983). Earthquake frequency distribution and the mechanics of faulting, *J. Geophys. Res.* **88,** 9331–9340.

Working Group on California Earthquake Probabilities (1988). Probabilities of large earthquakes occurring in California on the San Andreas fault, *U.S. Geological Survey Open-File Report*, 62 pp.

Working Group on California Earthquake Probabilities (1990). Probabilities of large earthquakes in the San Francisco Bay region, California, *U.S. Geological Survey Circular*, 51 pp..

Working Group on California Earthquake Probabilities (1995). Seismic hazards in southern California: Probable earthquakes, 1994–2024, *Bull. Seismol. Soc. Am.* **85,** 379–439.

Working Group on California Earthquake Probabilities (2003). Earthquake probabilities in the San Francisco Bay region: 2002–2031, *USGS Open-File Report 2003-214*, 235 pp;p.

Working Group on California Earthquake Probabilities (2008). The Uniform California Earthquake Rupture Forecast, version 2 (UCERF 2), *USGS Open-File Report 2007-1437, and California Geological Survey Special Report 203*, 96 pp.

Youngs, R. R., W. J. Arabasz, R. E. Anderson, A. R. Ramelli, J. P. Ake, D. B. Slemmons, J. P. McCalpin, D. I. Doser, C. J. Fridrich, F. H. Swan III, A. M. Rogers, J. C. Yount, L. W. Anderson, K. D. Smith, R. L. Bruhn, P. L. K. Knuepfer, R. B. Smith, C. M. dePolo, D. W. O'Leary, K. J. Coppersmith, S. K. Pezzopane, D. P. Schwartz, J. W. Whitney, S. S. Olig, and G. R. Toro (2003). A methodology for probabilistic fault displacement hazard analysis (PFDHA), *Earthq. Spectra* **19,** 191–219.

U.S. Geological Survey
P.O. Box 25046, Mail Stop 966
Denver, CO 80225-0046
(E.H.F.)

U.S. Geological Survey
525 South Wilson Ave.
Pasadena, CA 91106-3212
(M.T.P.)

Manuscript received 4 January 2010